SCIENCE CHINA
Chemistry

•ARTICLES•
SPECIAL TOPIC: Precise Catalysis Science and Technology

July 2021 Vol.64 No.7: 1103–1110
https://doi.org/10.1007/s11426-020-9867-x

Atomically dispersed copper species on ceria for the low-temperature water-gas shift reaction

Jing Ning[1,2], Yan Zhou[1*] & Wenjie Shen[1*]

[1]*State Key Laboratory of Catalysis, Dalian Institute of Chemical Physics, Chinese Academy of Sciences, Dalian 116023, China;*
[2]*University of Chinese Academy of Sciences, Beijing 100049, China*

Received July 6, 2020; accepted September 7, 2020; published online October 15, 2020

The structure of copper species, dispersed on nanostructured ceria (particles, rods and cubes), was analyzed by scanning transmission electron microscopy (STEM) and X-ray photoelectron spectroscopy (XPS). It was interestingly found that the density of surface oxygen vacancies (or defect sites), induced by the shape of ceria, determined the geometrical structure and the chemical state of copper species. Atomically dispersed species and monolayers containing few to tens of atoms were formed on ceria particles and rods owing to the enriched anchoring sites, but copper clusters/particles co-existed, together with the highly dispersed atoms and monolayers, on cubic ceria. The atomically dispersed copper sites and monolayers interacted strongly with ceria, involving a remarkable charge transfer from copper to ceria at their interfaces. The activity for the low-temperature water-gas shift reaction of the Cu/CeO_2 catalysts was associated with the fraction of the positively-charged copper atoms, demonstrating that the active sites could be tuned by dispersing Cu species on shape-controlled ceria particles.

Cu/CeO_2 catalysts, ceria shape, copper-ceria interface, atomically dispersed copper sites, monolayers, low-temperature water-gas shift reaction

Citation: Ning J, Zhou Y, Shen W. Atomically dispersed copper species on ceria for the low-temperature water-gas shift reaction. *Sci China Chem*, 2021, 64: 1103–1110, https://doi.org/10.1007/s11426-020-9867-x

1 Introduction

Cu/CeO_2 catalysts are reported to be highly active for the low-temperature water-gas shift (WGS) reaction [1–3], where the copper-ceria interfaces, in the model or inverse CeO_2/Cu systems [1,4,5] and the real powder Cu/CeO_2 catalysts [2,3,6–12], have been verified to be largely responsible for the activity. In most cases, the reaction occured at the copper-ceria interfacial perimeter: the copper site adsorbs CO chemically and the oxygen vacancy site nearby activates H_2O dissociatively [10]. The strong interaction between copper and ceria proceeds in a synergistic manner: ceria disperses and stabilizes the copper species while the copper species alter the redox feature of ceria *via* charge transfer. That is, the copper-ceria interface is determined by the surface properties of ceria and the dispersion of copper species. More specifically, the surface oxygen vacancy, relating to the number of Ce^{3+} on ceria, governed by the particle size/shape, served as the anchoring site for copper species, while their interfacial bonding pattern determined the dispersion and chemical state of the copper species [6,9,10–16]. Therefore, enriching oxygen vacancies, by tuning the particle size/shape of ceria, has been popularly adopted to maximize the metal-support interfacial perimeter for enhancing the catalytic efficiency.

The surface characters of ceria strongly affect the adhesion energy of copper species and thereby the copper-ceria interfacial structure [17–21]. For a specific loading amount of copper (1.0 wt%–8.5 wt%), ceria rods, as compared with the spherical particles and cubes, exhibited unique interactions

*Corresponding authors (email: zhouyan@dicp.ac.cn; shen98@dicp.ac.cn)

with copper species due to the preferential exposure of the {110}/{100} or {111}/{100} facets [7,13,14,16], and displayed higher activities for N_2O decomposition [13], CO_2 hydrogenation [14], CO oxidation [16,22,23] and NO reduction by CO [24]. For example, at a copper loading of 4.0 wt%, copper particles of 1.5–4.5 nm, together with clusters containing few copper atoms, distributed on ceria rods and particles, while copper particles ranging from 3 to 15 nm located on cubic ceria [13]. The former showed a higher activity towards N_2O decomposition because of the higher dispersion of copper and the facilitated mobility of oxygen species on the reactive {110}/{100} facets of ceria. Similarly, copper monolayers/bilayers of 1–2 nm dominated on ceria rods and particles whereas mainly copper particles of 2–5 nm presented ceria cubes in a 3.3 wt% CuO/CeO_2 system; the highly dispersed copper oxide species on ceria rods and particles showed a higher activity toward CO oxidation [16]. However, it was also observed that Cu clusters and particles, with copper loadings of 1.0 wt%–10 wt%, dispersed on ceria spheres [6,8] and octahedron [9], both exposing the {111} facets. The ceria spheres stabilized smaller copper particles and facilitated the dissociation of water, resulting in a higher activity towards the low-temperature WGS reaction. Copper species dispersed on spherical and cubic ceria, with a copper loading of 1.0 wt%, were reported to be more active for CO oxidation [25] and the preferential oxidation of CO in hydrogen-rich stream [26] than that over ceria rods, primarily due to the strong copper-ceria interaction.

We have recently identified that rod-shaped ceria favored the dispersion of copper monolayers and bilayers at a copper loading of 3.4 wt% [10], while further increasing the amount of copper resulted in multi-layered clusters and faceted particles [11]. By dispersing nearly identical amount (around 3.4 wt%) of copper on nanostructured ceria, we have found that the rod-shaped and spherical ceria favored the presence of copper oxide monolayers and bilayers but the cubic ceria led to the co-existence of CuO_x multilayers and faceted particles [16]. However, the atomic structure of the copper species and the relevant copper-ceria interfaces, especially these over the cubic and spherical ceria, remains less known. In this work, we extended to examine the dispersion patterns of copper species on ceria particles, rods and cubes by further lowering the amount of copper to around 1.6 wt% in order to assure that the ceria surface has enough anchoring sites to bond the copper species. It was interestingly found that copper presented mainly as atomically dispersed species on ceria particles while atoms and monolayers on ceria rods, but copper clusters and particles (2–5 nm), together with atomically dispersed atoms and monolayers, located on ceria cubes. The interaction manner of the dispersed copper species with the nanostructured ceria was unambiguously verified at the atomic scale and quantitatively correlated with their catalytic activity for the low-temperature WGS reaction.

2 Experimental

2.1 Preparation of the catalysts

Ceria particles, rods and cubes were prepared by an aqueous-phase precipitation or the hydrothermal synthesis, while the Cu/CeO_2 samples were prepared using a deposition-precipitation method, as we previously described [16]. Briefly, 0.1 g $Cu(CH_3COO)_2{\cdot}2H_2O$ was dissolved into 10 mL water and 2.0 g ceria was added at room temperature under stirring; 5 mL 0.1 M K_2CO_3 aqueous solution was then added dropwise with a final pH value of 8.0, and the mixture was further aged for 2 h. The precipitate was filtrated, washed with water and ethanol, dried at 80 °C overnight under vacuum and finally calcinated at 300 °C for 3 h in air. Hydrogen reduction of the as-calcinated CuO/CeO_2 samples at 300 °C for 2 h yielded the Cu/CeO_2 catalysts. The amounts of copper in the samples were around 1.6 wt%, as determined by the inductively coupled plasma atomic emission spectroscopy (ICP-AES) on an ICPS-8100 spectrometer. Based on the shape of ceria, the samples were labeled as CuO-/Cu-P, CuO-/Cu-R and CuO-/Cu-C, where P, R and C referred to ceria particles, rods and cubes.

2.2 Structure characterizations

The X-ray diffraction (XRD) pattern of the sample was taken over a D/Max-2500/PC diffractometer (Rigaku) using a Cu Kα radiation source (40 kV and 200 mA). The crystallite size of ceria in the sample was estimated, using the Scherrer's equation, from the half-width of the typical (111) line.

The temperature-programmed reduction of the CuO/CeO_2 sample by hydrogen (H_2-TPR) was performed using an Autochem II 2920 system (Micromeritics). Before the measurement, the CuO/CeO_2 (100 mg) sample was treated with a 20 vol% O_2/N_2 stream (30 mL min^{-1}) at 300 °C for 1 h for removing any surface impurities, and then cooled down to room temperature by Ar flowing (30 mL min^{-1}). The sample was then heated to 500 °C at a rate of 1 °C min^{-1} under the flow of a 2 vol% H_2/Ar mixture (30 mL min^{-1}). The consumption of hydrogen was monitored by a thermal conductive detector.

The high angle annular dark field scanning transmission electron microscopy (HAADF-STEM) images were recorded over a JEOL ARM 300F microscope (300 kV). The powder sample was ultrasonically dispersed into ethanol, and the droplets of the suspensions were deposited onto a carbon-coated Cu or Au grid and dried in air.

The X-ray photoelectron spectroscopy (XPS) measurement was done with a ThermoFisher ESCALAB250xi XPS

analyzer that equipped with a monochromatic Al Kα X-ray source. The CuO/CeO_2 sample, which was pressed into a thin disc, was reduced into Cu/CeO_2 in the pretreatment chamber with a 5 vol% H_2/N_2 mixture at 300 °C for 2 h. The spectra of Cu 2p, Cu L_3VV, Ce 3d and O 1s were then recorded in the analysis chamber. The charging effect was adjusted setting the binding energy of Ce 3d (v) at 882.5 eV.

2.3 Catalytic tests

The low-temperature WGS reaction was tested using a continuous-flow fixed-bed microreactor under atmospheric pressure. 100 mg CuO/CeO_2 (40–60 mesh) was loaded into the reactor and pre-treated with a 20 vol% O_2/N_2 mixture (30 mL min^{-1}) at 300 °C for 1 h. Then, it was reduced by hydrogen (5 vol% H_2/N_2, 30 mL min^{-1}) at 300 °C for 2 h. The feed gas (1.0 vol% CO/3.0 vol% H_2O/He, 67 mL min^{-1}) was introduced into the reactor, and the reaction was tested for about 12 h. The outlet from the reactor was analyzed with an online gas chromatograph (Agilent 7890A) equipped with a thermal conductivity detector and a flame ionization detector. The reaction rates at 200 °C were measured by controlling the conversion of CO below 10% *via* changing the flow rate of the reaction gases or the weight of the catalyst.

3 Results and discussion

3.1 Copper oxides on ceria

The diffraction lines in the XRD patterns of the CuO/CeO_2 samples were indexed to the cubic fluorite phase of ceria (Figure 1). The crystalline size of ceria followed the order of CuO-C (22.9 nm)>CuO-R (12.8 nm)>CuO-P (8.9 nm), giving the surface area of 37.2, 102.4 and 126.1 $m^2 g^{-1}$, respectively. As compared with pure ceria (Figure S1, Supporting Information online), the lattice parameters of the CuO/CeO_2 samples decreased only slightly. This is usually attributed to the chemical interaction of CuO with ceria during calcination in air, forming Ce_{1-x}-Cu_xO_2 solid solutions on ceria surface and altering the concentration of surface Ce^{4+} species [23,27]. The absence of diffraction lines of CuO indicated the highly dispersed, small copper oxides on ceria.

STEM analysis verified the dispersion of copper oxides on the nanostructured ceria. The CuO-P sample had a polyhedral morphology with an average size of about 9 nm; atomically dispersed copper atoms and monolayers presented on the {111} and {100} surfaces of ceria (Figure 2(a)). The CuO-R sample had a rod-shaped morphology, 10 nm wide and 150 nm long, exposing the {111} and {100} facets; the substantial voids (2–5 nm) inside the ceria rods indicated the abundant defects including edges and terraces that are rich in oxygen vacancies and Ce^{3+} (Figure 2(b)). Concerning the dispersion of copper oxides, atomically

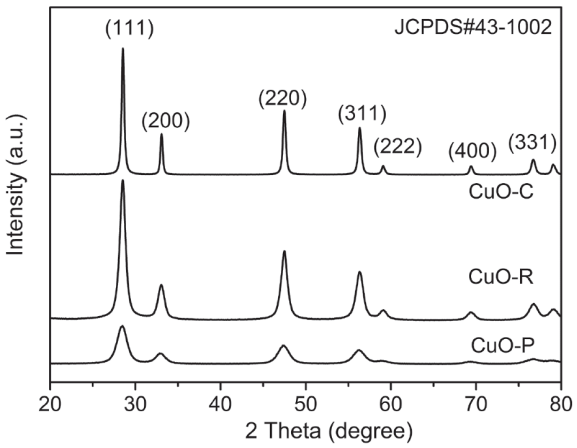

Figure 1 XRD patterns of the CuO/CeO_2 samples.

dispersed species, monolayers and bilayers simultaneously presented on the surface of ceria. The CuO-C sample had an average size of 21.1 nm and exposed mainly the {100} planes with minor {110} planes (consisting of {111} facets) at the edges and {111} plane at the corners (Figure 3). Copper presented in the forms of atomically dispersed species and monolayers while clusters were also observed occasionally. When viewed along the [001] direction, copper thin-layers and clusters were identified on the {100} facets; atomically dispersed species and copper monolayers were seen on the {111} facets at the corners and edges as viewed along the [110] direction. ABF-STEM images, viewed along the [001] direction, showed the location of oxygen atoms and oxygen vacancies on CeO_2 (100) surface (Figure S2). It seems that the nanostructured ceria provided anchoring sites for dispersing copper oxides, in the forms of atomically dispersed species, monolayers and clusters, depending on the surface area that is associated with the shape of ceria particles.

According to a theoretical model by assuming that all the cation vacancies on CeO_2 {111} planes could be replaced by Cu^{2+} [28], the critical value of Cu^{2+} for a monolayer dispersion on ceria is 1.22 mmol/100 m^2. Here, the ceria cubes, with a surface area of 37.2 $m^2 g^{-1}$, would allow a monolayer dispersion of 3.7 wt% Cu if their surface bonding is strong enough. Therefore, the appearance of copper clusters on CuO-C is not due to the lower surface area as compared to CuO-P and CuO-R. Instead, it probably stems from the lower population of oxygen vacancies or defects that anchored copper species.

3.2 Hydrogen-reduction of the CuO/CeO_2 samples

The impact of ceria shape on the reduction property of the dispersed copper oxides was elucidated by the H_2-TPR profiles (Figure 4). Generally, the reduction of CuO/CeO_2

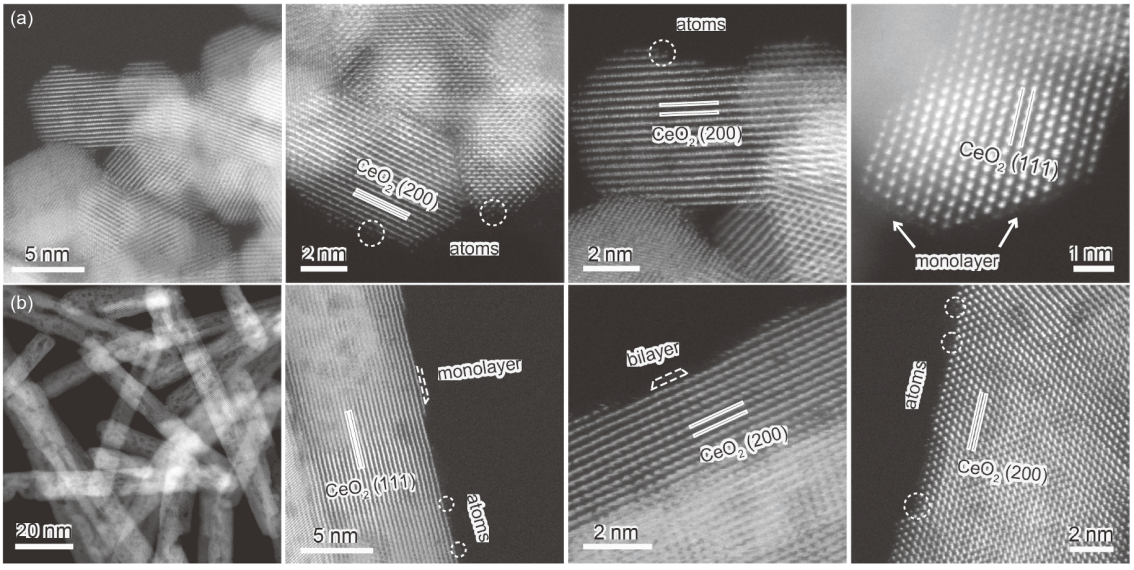

Figure 2 STEM images of the CuO-P (a) and CuO-R (b) samples.

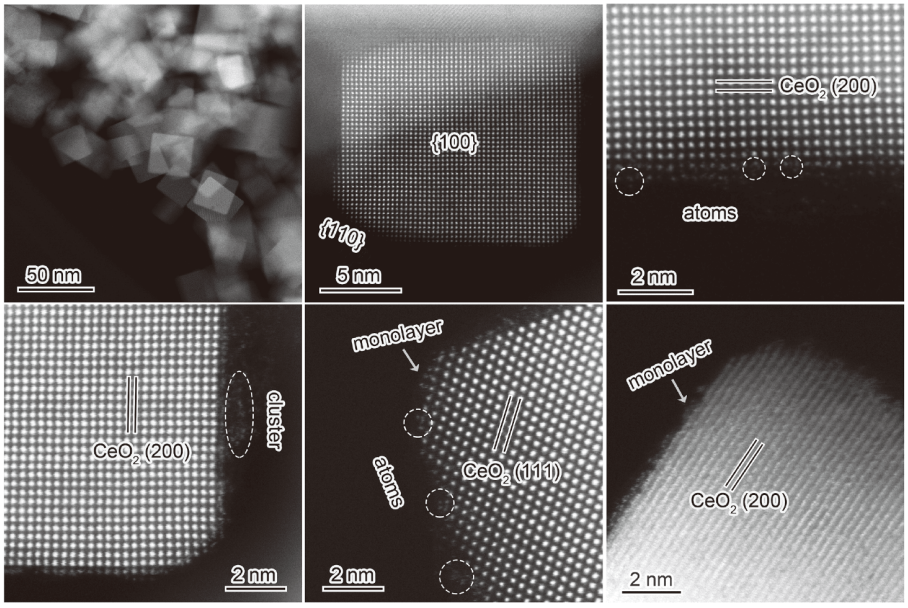

Figure 3 Representative STEM images of the CuO-C sample.

occurred at much lower temperatures than those for CuO [28] and ceria [10,15], primarily because the copper-ceria interaction greatly promotes their reductions by hydrogen. Specifically, the reduction of the CuO-P sample was featured by two distinct steps centered at 91.9 and 111.3 °C. The former referred to the collective conversion of atomically dispersed species/monolayers, together with the partial reduction of surface ceria (β), while the latter represented the surface reduction of ceria promoted by copper (γ) [7,16,28–30]. The reduction of CuO-R was similar to that of CuO-P, showing distinct reduction peaks at 111.5 and 128.6 °C. On the CuO-C sample, an additional peak appeared at 112.0 °C (α), presenting the reduction of CuO clusters that might interact with ceria relatively weakly [31].

The amount of hydrogen consumed, with respect to the copper oxide species, was estimated (Table 1). The total amount of H_2 consumed was much higher than the theoretical value for converting CuO to Cu^0 in the samples, evidencing the combined reduction of copper oxides and ceria surface [7,12,16,28–32]. This character was more remarkable on ceria particles and rods. Moreover, copper oxide monolayers and atomically dispersed copper species on ceria rods and particles consumed much more hydrogen than the clusters on ceria cubes, indicating the higher dispersion of

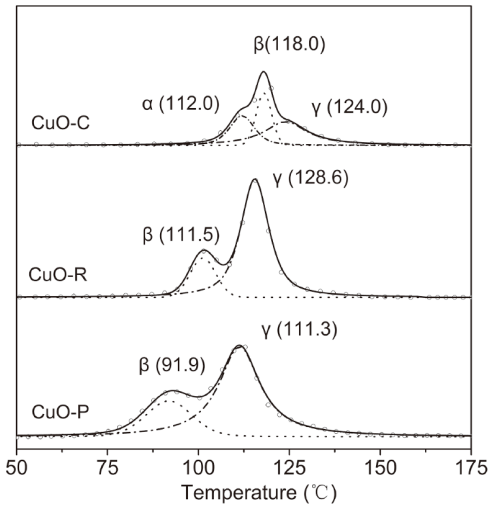

Figure 4 H_2-TPR profiles of the CuO/CeO_2 samples.

copper oxides. The CuO_x clusters on cubic ceria were readily reduced at lower temperatures due to the weaker bonding with ceria [31], while the atomically dispersed species/monolayers were reduced at moderate temperatures because of the strong bond to ceria at the copper-ceria interfaces. Their reduction was accompanied by the reduction of surface ceria promoted by copper. Accordingly, the Cu/CeO_2 catalysts, for the low-temperature WGS reaction, were obtained by hydrogen-reduction of the CuO/CeO_2 precursors at 300 °C.

3.3 Structure properties of the Cu/CeO_2 catalysts

The geometric structure of the copper species dispersed on ceria was identified by STEM observations. On ceria particles and rods (Figure 5), copper presented in the forms of atomically dispersed species and monolayers. More specifically, mainly atomically dispersed copper located on ceria particles, while both atoms and monolayers presented on ceria nanorods. On ceria cubes (Figure 6), besides monolayers and atomically dispersed species, Cu clusters (around 2 nm) and particles (3–5 nm) located on the {100} plane and the {111} facet at the corners. The lattice spacing of 0.21 and 0.18 nm, with a dihedral angle of 54.7°, represented Cu {111} and {200} facets, respectively, affirming the crystalline nature of the Cu particles. Atomically dispersed species and monolayers dominated on the surfaces of ceria cubes while the fraction of Cu clusters and particles was less than 10%.

The chemical environments of the dispersed copper species in the Cu/CeO_2 catalysts were examined by XPS (Figure 7). The binding energies of Cu $2p_{3/2}$ and Cu $2p_{1/2}$ at 932.7 and 952.4 eV, respectively, together with absence of the satellite peak in-between, indicated that the Cu^{2+} were reduced to Cu^0 and Cu^+ [33–35]. The minor shoulder peaks at 929.3 eV in the Cu-P and Cu-R samples were ascribed to the interfacial Cu^+ close to the oxygen vacancies [34]. The Cu Auger L_3VV spectra discriminated the Cu^0 and Cu^+ species. The kinetic energy at 918.3 eV corresponded to Cu^0 while that at 915.9 eV represented Cu^+ [33,35]. A semi-quantitative analysis indicated that Cu^+ was dominant in the three catalysts, demonstrating that most copper species presented as Cu^+ that was stabilized by ceria. It is most likely that the Cu^+ atoms strongly interacted with the oxygen vacancy on ceria, forming a Ce^{3+}-O_V-Cu^+ interfacial bonding, while the Cu^0 atoms directly coordinated with the neighboring Cu^+ atoms in the clusters/particles [3,10]. The dispersion of copper species on ceria heavily relies on the competition between the interfacial Cu–O–Ce bond and the intra-particle Cu–Cu bond, which is intimately linked to the coverage of copper and the reduction degree of ceria surface [17–21]. Theoretical simulations have demonstrated that the bonding energy of copper atoms on the reduced ceria surface, *i.e.*, the interfacial Cu–O–Ce bond, is comparable to that of the Cu–Cu bond in copper clusters [17,18]. Both experimental investigations and theoretical calculations have verified that the interfacial Cu–O–Ce bonding was governed by the coverage of copper and the density of oxygen vacancies (defect sites) of ceria [19–21]. Here, the much lower amount of copper (1.6 wt%) and the significantly enriched oxygen vacancies on the spherical and rod-shaped ceria, as evidence by H_2-TPR and XPS data, acted as the driving forces for the atomic and monolayer dispersion of copper with the interfacial bonding of Ce^{3+}–O_V–Cu^+; while the relative less defects on cubic ceria led to the formation of copper clusters *via* Cu–Cu bonding, in addition to the atomically dispersed sites and monolayers.

The XPS of Ce 3d in the Cu/CeO_2 catalysts were deconvoluted into eight peaks with the binding energy ranging from 875 to 925 eV (Figure 8). They were classified into two types of spin-orbital multiplets for $3d_{3/2}$ and $3d_{5/2}$, and de-

Table 1 Amounts of consumed hydrogen as derived from the H_2-TPR profiles of the CuO/CeO_2 samples

Sample	Copper loading (wt%)	Consumed hydrogen (μmol g^{-1})/temperature (°C)			Total amount of consumed hydrogen (μmol g^{-1})	Theoretical value (μmol g^{-1}) [a)]
		α	β	γ		
CuO-P	1.6	–	176.7/91.9	593.5/111.3	770.2	124.8
CuO-R	1.5	–	109.1/111.5	571.0/128.6	680.1	115.7
CuO-C	1.6	75.3/112.0	64.0/118.0	142.9/124.0	282.2	121.8

a) Calculated from the actual loading of copper and by assuming as CuO.

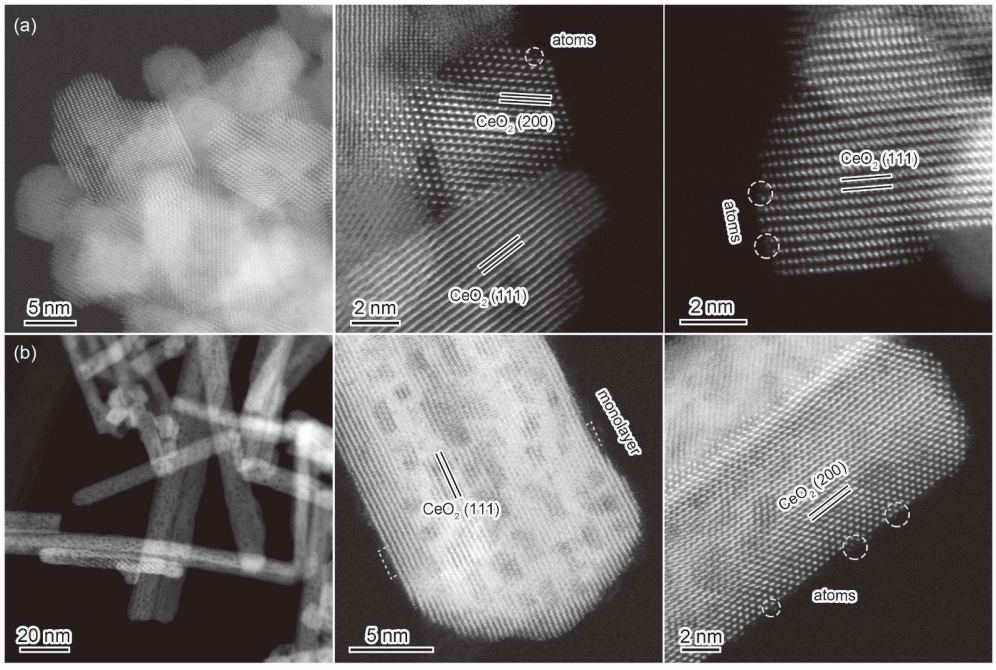

Figure 5 STEM images of the Cu-P (a) and Cu-R (b) catalysts.

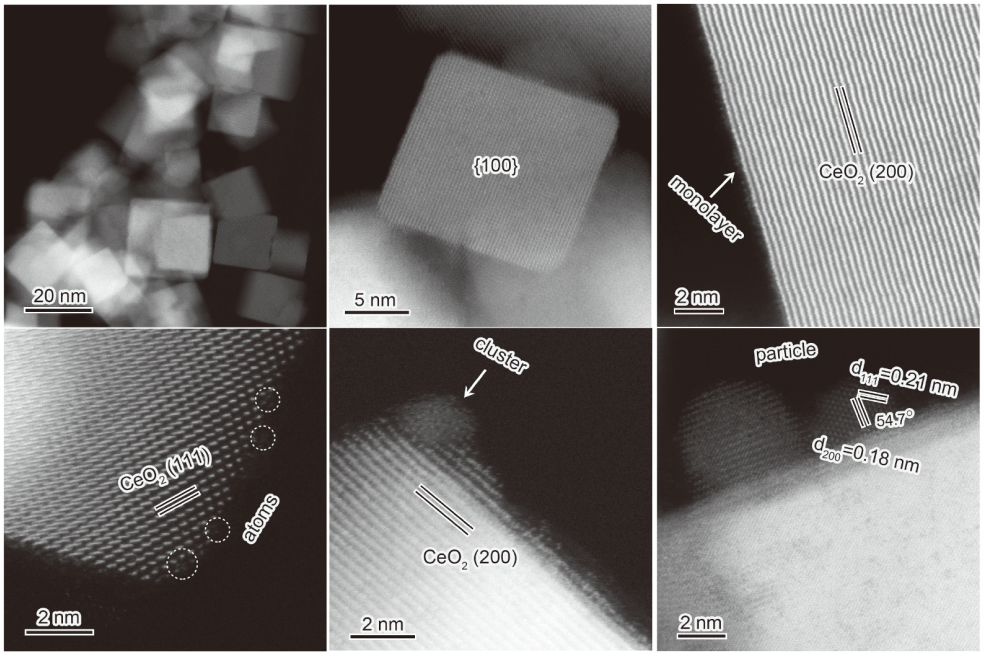

Figure 6 STEM images of the Cu-C catalyst.

noted as u and v. The u′ and v′, u^0 and v^0 peaks corresponded to Ce^{3+} while the u‴ and v‴, u″ and v″, u and v peaks referred to Ce^{4+} [9,10,15]. The concentration of surface Ce^{3+}, which is intimately associated with surface oxygen vacancies [36], was estimated from the intensities of the u^0 (v^0) and u′ (v′) peaks relative to the total intensity of Ce 3d. It was 27% in Cu-P, 22% on Cu-R and 18% on Cu-C. In the XPS of O 1s, the major binding energy at 529.2 eV was ascribed to lattice oxygen (O_I) and the minor binding energy at 531.2 eV was assigned to the weakly adsorbed oxygen species (O_{II}) captured by the oxygen vacancies [10,15,27]. Accordingly, the concentration of oxygen vacancies was estimated to be 23% on Cu-P, 20% on Cu-R and 15% on Cu-C, following the same trend with that of Ce^{3+}.

As compared with the as-calcined CuO/CeO_2 samples (Figure S3), hydrogen reduction at 300 °C has converted the

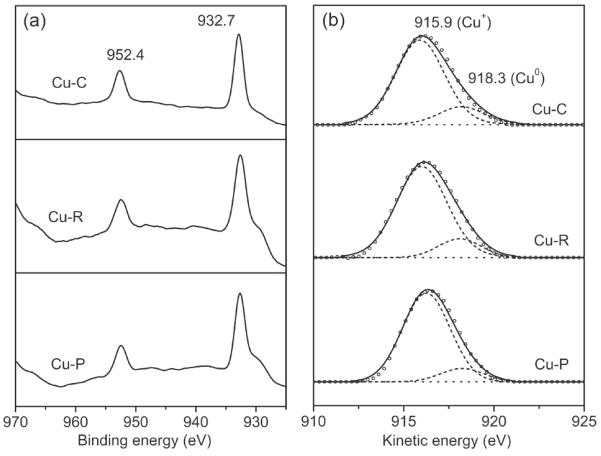

Figure 7 XPS of Cu 2p (a) and Cu Auger L_3VV (b) in the Cu/CeO_2 catalysts.

Cu^{2+} species into Cu^+ and Cu^0; while the fractions of Ce^{3+} species and oxygen vacancies increased moderately, mainly derived from the reduction of ceria surfaces. These results are in good agreement with the H_2-TPR and STEM data that demonstrated the variations in the redox properties of ceria and the dispersion of copper species. The Cu^+ species stem from the reduction of the Cu^{2+} [37] and strongly interact with oxygen vacancies on ceria, forming the interfacial Cu^+–O_V–Ce^{3+} bonding *via* a charge transfer from copper to ceria [17].

3.4 Catalytic activities for the low-temperature WGS reaction

The Cu/CeO_2 catalysts were then tested for the low-temperature WGS reaction at 200 °C (Figure 9). The conversion of CO, taking the average for about 12 h, was 32% on Cu-P, moderately declined to 26% over Cu-R and 21% on Cu-C. The slight loss of the activity at the initial stage was probably due to the aggregation of the atomically dispersed species and monolayers. The reaction rate was 1.4×10^{-4} mol_{CO} g_{Cu}^{-1} s^{-1} on Cu-P, decreased to 0.8×10^{-4} mol_{CO} g_{Cu}^{-1} s^{-1} on Cu-R and 0.5×10^{-4} mol_{CO} g_{Cu}^{-1} s^{-1} over Cu-C. Apparently, the Cu-P catalyst is more active than the other two architectures, affirming the intrinsically higher activity of the atomically dispersed copper sites determined by the surface properties of the spherical ceria. This agrees well with the variation in the population of atomically dispersed sites, monolayers and clusters/particles by varying the shape of ceria. Previous studies on copper dispersion over ceria have found that ceria particles, enclosed by the {111} facets, could efficiently stabilize highly dispersed Cu speices and thus generate more active sites for the low-temperature WGS reaction at the copper-ceria interfaces [6,8,9]. Here, the activity order, Cu-P>Cu-R>Cu-C, is approximately in line with the concentration of Cu^+ in the atomically dispersed sites and monolayers, strongly suggesting that the interfacial Cu^+–O_V–Ce^{3+} served as the active sites [4,10,11,38]. The oxygen vacancy in connection with the positively-charged copper facilitates water dissociation, as the rate-determining step, and the Cu^+ site adsorbs and activates CO that would be directly oxidized by the adjunct activated water species [10].

4 Conclusions

The shape effect of nanostructured ceria on the dispersion of copper species, at a lower copper loading level (1.6 wt%), was investigated. Spherical and rod-shaped ceria, with densely populated surface oxygen vacancies, tightly bonded the copper species as atomically dispersed sites and monolayers; while cubic ceria resulted in the co-existence of atoms, monolayers and clusters/particles because of the relatively weaker copper-ceria interaction. The atomically dispersed copper site was effectively stabilized on ceria by forming the interfacial Cu^+–O_V–Ce^{3+} bond *via* a charge transfer from copper to ceria. The population variation among atoms, monolayers and clusters/particles, induced by the shape of

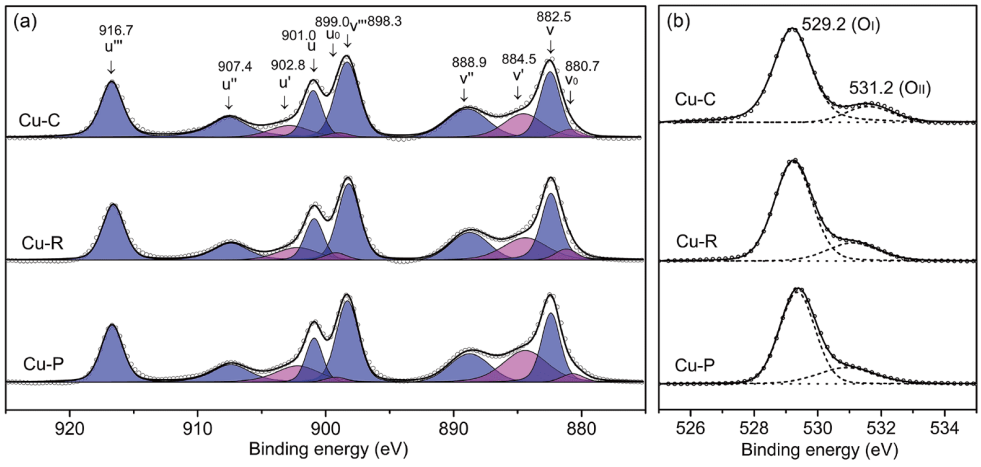

Figure 8 XPS of Ce 3d (a) and O 1s (b) in the Cu/CeO_2 catalysts (color online).

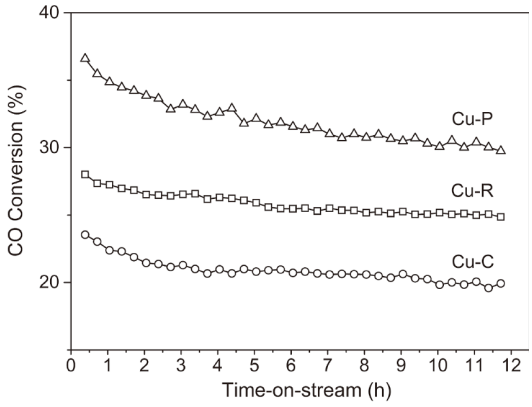

Figure 9 Low-temperature WGS reaction over the Cu/CeO_2 catalysts at 200 °C. Reaction conditions: 1.0 vol% CO/3.0 vol% H_2O/He, 40,000 h^{-1}.

ceria, was correlated with the catalytic activity for the low-temperature WGS reaction. The atomically dispersed copper species and monolayers were intrinsically more active than the copper clusters/particles, probably because of the facilitated activation of water and CO on the interfacial Cu^{+}-O_V-Ce^{3+} sites: CO chemically adsorbs on Cu^{+} while H_2O dissociatively activates on the neighboring oxygen vacancy.

Acknowledgements This work was supported by the National Natural Science Foundation of China (21761132031, 21533009).

Conflict of interest The authors declare no conflict of interest.

Supporting information The supporting information is available online at http://chem.scichina.com and http://link.springer.com/journal/11426. The supporting materials are published as submitted, without typesetting or editing. The responsibility for scientific accuracy and content remains entirely with the authors.

1 Senanayake SD, Stacchiola D, Rodriguez JA. *Acc Chem Res*, 2013, 46: 1702–1711
2 Konsolakis M. *Appl Catal B-Environ*, 2016, 198: 49–66
3 Zhou Y, Chen A, Ning J, Shen W. *Chin J Catal*, 2020, 41: 928–937
4 Rodriguez J , Graciani J, Evans J, Park J , Yang F, Stacchiola D, Senanayake S , Ma S, Pérez M, Liu P, Sanz J , Hrbek J. *Angew Chem*, 2009, 121: 8191–8194
5 Yan H, Yang C, Shao WP, Cai LH, Wang WW, Jin Z, Jia CJ. *Nat Commun*, 2019, 10: 3470
6 Gawade P, Mirkelamoglu B, Ozkan US. *J Phys Chem C*, 2010, 114: 18173–18181
7 Si R, Raitano J, Yi N, Zhang L, Chan SW, Flytzani-Stephanopoulos M. *Catal Today*, 2012, 180: 68–80
8 Yao SY, Xu WQ, Johnston-Peck AC, Zhao FZ, Liu ZY, Luo S, Senanayake SD, Martínez-Arias A, Liu WJ, Rodriguez JA. *Phys Chem Chem Phys*, 2014, 16: 17183–17195
9 Ren Z, Peng F, Li J, Liang X, Chen B. *Catalysts*, 2017, 7: 48
10 Chen A, Yu X, Zhou Y, Miao S, Li Y, Kuld S, Sehested J, Liu J, Aoki T, Hong S, Camellone MF, Fabris S, Ning J, Jin C, Yang C, Nefedov A, Wöll C, Wang Y, Shen W. *Nat Catal*, 2019, 2: 334–341
11 Ning J, Zhou Y, Chen A, Li Y, Miao S, Shen W. *Catal Today*, 2020, 357C: 460–467
12 May YA, Wang WW, Yan H, Wei S, Jia CJ. *Chin J Catal*, 2020, 41: 1017–1027
13 Zabilskiy M, Djinović P, Tchernychova E, Tkachenko OP, Kustov LM, Pintar A. *ACS Catal*, 2015, 5: 5357–5365
14 Lin L, Yao S, Liu Z, Zhang F, Li N, Vovchok D, Martínez-Arias A, Castañeda R, Lin J, Senanayake SD, Su D, Ma D, Rodriguez JA. *J Phys Chem C*, 2018, 122: 12934–12943
15 Zou Q, Zhao Y, Jin X, Fang J, Li D, Li K, Lu J, Luo Y. *Appl Surf Sci*, 2019, 494: 1166–1176
16 Ning J, Dong C, Li M, Zhou Y, Shen W. *J Chem Phys*, 2020, 152: 094708
17 Szabová L, Camellone MF, Huang M, Matolín V, Fabris S. *J Chem Phys*, 2010, 133: 234705
18 Yang Z, Xie L, Ma D, Wang G. *J Phys Chem C*, 2011, 115: 6730–6740
19 James TE, Hemmingson SL, Ito T, Campbell CT. *J Phys Chem C*, 2015, 119: 17209–17217
20 James TE, Hemmingson SL, Campbell CT. *ACS Catal*, 2015, 5: 5673–5678
21 Chen S, Li L, Hu W, Huang X, Li Q, Xu Y, Zuo Y, Li G. *ACS Appl Mater Interfaces*, 2015, 7: 22999–23007
22 Zhou K, Xu R, Sun X, Chen H, Tian Q, Shen D, Li Y. *Catal Lett*, 2005, 101: 169–173
23 Lykaki M, Pachatouridou E, Carabineiro SAC, Iliopoulou E, Andriopoulou C, Kallithrakas-Kontos N, Boghosian S, Konsolakis M. *Appl Catal B-Environ*, 2018, 230: 18–28
24 Liu L, Yao Z, Deng Y, Gao F, Liu B, Dong L. *ChemCatChem*, 2011, 3: 978–989
25 Wang WW, Yu WZ, Du PP, Xu H, Jin Z, Si R, Ma C, Shi S, Jia CJ, Yan CH. *ACS Catal*, 2017, 7: 1313–1329
26 Gamarra D, Cámara AL, Monte M, Rasmussen SB, Chinchilla LE, Hungría AB, Munuera G, Gyorffy N, Schay Z, Corberán VC, Conesa JC, Martínez-Arias A. *Appl Catal B-Environ*, 2013, 130-131: 224–238
27 Piumetti M, Bensaid S, Andana T, Russo N, Pirone R, Fino D. *Appl Catal B-Environ*, 2017, 205: 455–468
28 Dong L, Yao X, Chen Y. *Chin J Catal*, 2013, 34: 851–864
29 Tang X, Zhang B, Li Y, Xu Y, Xin Q, Shen W. *Appl Catal A-General*, 2005, 288: 116–125
30 Luo MF, Song YP, Lu JQ, Wang XY, Pu ZY. *J Phys Chem C*, 2007, 111: 12686–12692
31 Gao Y, Zhang Z, Li Z, Huang W. *Chin J Catal*, 2020, 41: 1006–1016
32 Freund HJ, Heyde M, Kuhlenbeck H, Nilius N, Risse T, Schmidt T, Shaikhutdinov S, Sterrer M. *Sci China Chem*, 2020, 63: 426–447
33 Qi L, Yu Q, Dai Y, Tang C, Liu L, Zhang H, Gao F, Dong L, Chen Y. *Appl Catal B-Environ*, 2012, 119-120: 308–320
34 Monte M, Munuera G, Costa D, Conesa JC, Martínez-Arias A. *Phys Chem Chem Phys*, 2015, 17: 29995–30004
35 Wang C, Cheng Q, Wang X, Ma K, Bai X, Tan S, Tian Y, Ding T, Zheng L, Zhang J, Li X. *Appl Surf Sci*, 2017, 422: 932–943
36 Li X, Liu K, Wang W, Bai X. *Sci China Chem*, 2019, 62: 1704–1709
37 Wang Y, Chen Z, Han P, Du Y, Gu Z, Xu X, Zheng G. *ACS Catal*, 2018, 8: 7113–7119
38 Wang X, Rodriguez JA, Hanson JC, Gamarra D, Martínez-Arias A, Fernández-García M. *J Phys Chem B*, 2006, 110: 428–434